nature communications

Article

https://doi.org/10.1038/s41467-025-64351-9

Single atom activated multi-stage active sites for thoroughgoing sodium utilization

Received: 5 September 2024

Accepted: 9 September 2025

Published online: 20 October 2025

Check for updates

Shengyong Gao[1,2,7], Yibo Zhu[1,7], Ke Shi[1], Peng Liu[1], Yiming Zhang[2], Junping Hu[3] ✉, Zhenhai Wen[4], Lina Wang[4,5] ✉, Wen Tan[5], Lianzhou Wang[2,6], Bin Luo[2] ✉ & Jisheng Zhou[1] ✉

Atomically dispersed metals offer advantages in guiding sodium deposition, yet the effects of single atoms on their surrounding structures and the precise tuning of coordination-governed single-atom activity remain underexplored. Herein, carbon nanofiber films with tin single atoms anchored via a dynamic coordination mode (shifting from coordination with three nitrogen atoms and one oxygen atom to coordination with one nitrogen atom and three oxygen atoms) are developed to address these challenges. The tin atoms not only enhance the sodium-ion adsorption activity of their directly coordinated nitrogen and oxygen atoms but also activate remote carbon atoms. The activation capability is strongly dependent on coordination environment, with tin atoms coordinated to more nitrogen atoms exhibiting higher activity. As a result, the optimized tin–carbon host enables uniform sodium deposition and complete stripping, allowing symmetric cells to cycle stably for 1200 h at 100 mA cm^{-2} and 100 mAh cm^{-2} with 100% depth of discharge. Anode-free full cells pairing the tin-carbon host with a sodium vanadate phosphate cathode achieve 94% capacity retention after 700 cycles at 10 C (6 min).

Accompanied by the leapfrog progress of clean energy harvest systems, the development of high-performance energy storage devices with low cost has become a topic of common concern[1,2]. Sodium-based batteries have emerged as promising alternatives to lithium batteries due to their nonnegligible cost advantages[3,4]. Sodium metal is considered as the ultimate selection for the development of anode materials because of its high theoretical specific capacity (1166 mA h g^{-1}) and low redox potential (−2.714 V)[5,6]. While it is laborious to achieve high-dimensional Na homomorphism deposition, leading to pathetic safety and stability of sodium batteries, arising from dendrites, dead sodium, volume variation, and side reactions[7].

Enhancing battery durability hinges primarily on supplying an excess of sodium source to counteract sodium loss[8]. Despite the implementation of some electrodes with extended cycle life, maintaining depth of discharge (DoD) and N/P ratio below the practical application thresholds inevitably comes at a cost. This diminishes the battery's energy density, rendering poor safety an unnecessary disadvantage compared to other advanced electrodes[9]. Anode-free, an ideal model where Na is exclusively sourced from the cathode, represents the ultimate goal for sodium metal anodes due to complete active sodium utilization[10,11]. However, achieving complete stripping and minimal side reactions between sodium and electrolyte proves

[1]State Key Laboratory of Chemical Resource Engineering, Beijing Key Laboratory of Electrochemical Process and Technology for Materials Technology, Beijing University of Chemical Technology, Beijing, PR China. [2]Australia Institute for Bioengineering and Nanotechnology (AIBN) & School of Chemical Engineering, The University of Queensland, Brisbane, QLD, Australia. [3]School of Science, Nanchang Key Laboratory of Photoelectric Conversion and Energy Storage Materials, Jiangxi University of Water Resources and Electric Power, Nanchang, PR China. [4]State Key Laboratory of Structural Chemistry, and Fujian Provincial Key Laboratory of Materials and Techniques toward Hydrogen Energy, Fujian Institute of Research on the Structure of Matter, Chinese Academy of Sciences, Fuzhou, PR China. [5]Fujian Key Laboratory of Green Extraction and High-Value Utilization of New Energy Metals, Fuzhou University, Fuzhou, PR China. [6]Department of Applied Biology and Chemical Technology, Faculty of Science, The Hong Kong Polytechnic University, Hong Kong SAR, PR China. [7]These authors contributed equally: Shengyong Gao, Yibo Zhu. ✉e-mail: jphu@nit.edu.cn; wanglina@fjirsm.ac.cn; b.luo1@uq.edu.au; zhoujs@mail.buct.edu.cn

challenging, leading to continuous electrolyte consumption based on the initial problem of difficult homomorphism deposition[12–14]. This results in, under practical DoD, low current density (e.g., <10 mA cm^{-2}) and areal capacity (e.g., <4 mA h cm^{-2}) are generally used for evaluating battery performances[15,16]. Strict conditions with practical significance are almost a luxury for electrodes designed for long-term operating.

Three-dimensional (3D) hosts, represented by carbon-based materials, demonstrated a unique advantage in guiding high-dimensional Na deposition and thus relieving volume change, enabling high deposition capacity[17–21]. In addition, assisted by dispersing local current density arising from regulated ion flux, deposition under high current densities is also possible to be implemented by 3D hosts. However, within the 3D carbon skeleton, the shorter diffusion path on the top surface and the concentration gradient along the thickness direction jointly contribute to sodium deposition being more inclined towards the side near the separator[22–24]. Moreover, under high current density, the chaotic deposition and dendritic growth caused by Na-phobic carbon matrix poses a challenge to the nucleation kinetics of sodium, causing the occurrence of battery failure due to the dendrite penetration of separator[23]. Consequently, the Na-phobic carbon skeletons struggle to support the rapid and uniform nucleation dynamics, i.e., loss the advantage in sodium carrying capacity under high current[24], which is the lifeblood of the design of 3D hosts[25].

Atomically dispersed metals ignite the hope of improving the poor sodiophilicity of carbon hosts[26–28]. Except coordination unsaturated rare-earth elements, e.g., Y[7], which reduce the nucleation energy barrier of sodium based on electron-rich 4f orbitals adsorption, transition metal M-N_4 structures (d-block, represented by Fe[29], Mn[30], Co[31], Ni[32], etc.) and p-block single atoms, such as Sn[15] and Bi[33], also demonstrate significant progress in guiding metal deposition. Among them, Sn shows a unique advantage. Due to the Na alloying reaction with Sn and the low nucleation energy barrier of Na on Sn metal, Sn metal is considered a sodiophilic substrate[34,35]. Space-confine the Sn to monodispersed clusters and further atomic level can fully utilize the Na-affinity of Sn[15,25]. Furthermore, single atom Sn has the $5s^25p^2$ orbital hybridization, which can guide the planar growth of Na clusters, further emphasizing the advantage of Sn[35]. Thus, carbon-supported Sn single atoms are supposed to guide reliable Na plating/stripping, acting as host materials.

Investigations towards the mechanisms of the enhanced Na nucleation on single-atom-modified carbon host have identified two aspects of cognition: (1) single atoms serve as active sites with significant adsorption advantages, turning the one-dimensional growth to smooth deposition[7]; (2) metal size that confined to atomic level permits complete alloy-dealloying, achieving high DoD and durability[15]. However, excessive focus on the intrinsic activity of single atomic sites obscure the contributions of other elements, which could be the underlying reason for the high activity observed in materials with low single-atom loading mass[36,37]. Heteroatoms, such as N, O, and P, typically serve as anchoring agents for single atoms, affecting the activity of metal centers[38]. Yet, it remains unexplored whether these heteroatoms act as nucleation sites in the presence of single atoms. Moreover, single atoms alter the electronic structure of the carbon matrix, which raises the question of whether the modified carbon skeleton is also activated as nucleation sites for sodium adsorption. Furthermore, difficulties lying in controlling the coordination mode hampers the in-depth exploration of the precise regulation of single atom activity, leaving the optimal coordination environment for maximizing the potential of metal centers remains unclear[39–44].

In this study, we report a series of free-standing carbon nanofiber films interspersed with diverse coordinated single Sn atoms to explore the metal-heteroatoms and metal-carbon interactions during Na plating/stripping. Beyond the intrinsic activity of single Sn atoms, the surrounding structure of Sn atoms also displays enhanced sodiophilicity due to Sn-induced activation. With the increase of Sn atoms anchored on the carbon texture, the coordination mode of Sn migrates from 3N-Sn-O to N-Sn-3O configuration. By optimizing the Sn coordination environment and activating the surrounding structure, the carbon hosts exhibit robust sodiophilicity, enabling symmetrical batteries to achieve stable cycling for over 1200 h under 100% Na utilization rate, high current density (100 mA cm^{-2}) and deposition capacity (100 mA h cm^{-2}). By integrating $Na_3V_2(PO_4)_3$ (NVP) cathode, anode-free full cells exhibit a stable cycle of 700 cycles under 10 C, indicating a promising prospect for the practical applications of single-Sn-atom-activated carbon matrices with optimized coordination.

Results

Fabrication and morphology of carbon nanofibers

The atomic Sn dispersed 3D carbon hosts were obtained by pyrolyzing polyacrylonitrile (PAN) nanofiber precursors containing $SnCl_2$ (Supplementary Fig. 1). The prepared carbon hosts were named as SnX@CNFs, where X represents the mass fraction of $SnCl_2$ in the precursor. The SnX@CNFs films display extraordinary flexibility, can even be folded as a boat shape (Fig. 1a and Supplementary Fig. 2) and maintain a 3D network from its precursor (Supplementary Fig. 3), which ensures the continuity of electronic transfer (Fig. 1b and Supplementary Fig. 4)[45]. The specific surface area of carbon hosts decreases with the rise of Sn content (Supplementary Fig. 5).

Single Sn atoms are dispersed in the disordered carbon matrix in SnX@CNFs. Wide peaks at around 24° corresponding to the (002) layer of disordered carbon texture appear in the powder X-ray diffraction (XRD) patterns (Fig. 2a) of all SnX@CNFs[46]. The amorphous structure can be confirmed by the high-resolution transmission electron microscopy (HRTEM, Fig. 1c, d and Supplementary Fig. 6) images and Raman spectra (Supplementary Fig. 7). The Sn dispersion state is determined by $SnCl_2$ mass fraction in the precursors (X). For $X \leq 30$, the absence of sharp diffraction peaks (Fig. 2a) indicates non-crystalline Sn, while for $X = 40$, the diffraction pattern of Sn crystal appears, consistent with Sn nanocrystals observed in the HRTEM image of Sn40@CNFs (Supplementary Fig. 6k), indicating the aggregation of Sn.

The isolated Sn atoms in SnX@CNFs ($X \leq 30$) can be directly visualized by (AC-STEM, Fig. 1e–g) with corresponding intensity profiles. The images of the sample edge can better reflect the state of Sn atoms in the carbon layer because of the smaller thickness, which presents as the independent bright spots uniformly dispersed in the carbon matrix. After processing the carbon samples into fiber tips by field ion beam (Fig. 1h and Supplementary Fig. 8), the atomic distribution of Sn, C, N, and O could be manifested by atom probe tomography (APT, Fig. 1i). The results demonstrate that all elements are well-dispersed throughout the fiber matrix, which is consistent with the high-angle annular dark-field scanning transmission electron microscope (HAADF-STEM) with energy-dispersive X-ray (EDX) elemental mapping (Supplementary Fig. 6).

According to X-ray photoelectron spectroscopy (XPS), the Sn content in carbon nanofibers rises with the increasing X (Supplementary Fig. 9a). Wherein, the value for Sn30@CNFs is 22.22 wt%, which is comparable to that obtained from EDX (19.72 wt%, Supplementary Table 1). Because of the residual carbon impurities, thermogravimetric (TG, Supplementary Fig. 10) test results have a positive bias (30.1 wt%). Besides, fluctuations in N and O content with increasing Sn content suggest the change of the Sn-coordination environment (Supplementary Fig. 9b, c). In general, when the Sn content is below approximately 20 wt%, the Sn atoms tend to remain in an atomic state.

Coordination structure of Sn atoms

Single Sn atoms are incorporated into the carbon skeleton through co-coordination with N and O atoms, and the fine coordination structure is determined by Sn content. By adjusting X from 10 to 40, the

https://doi.org/10.1038/s41467-025-64351-9

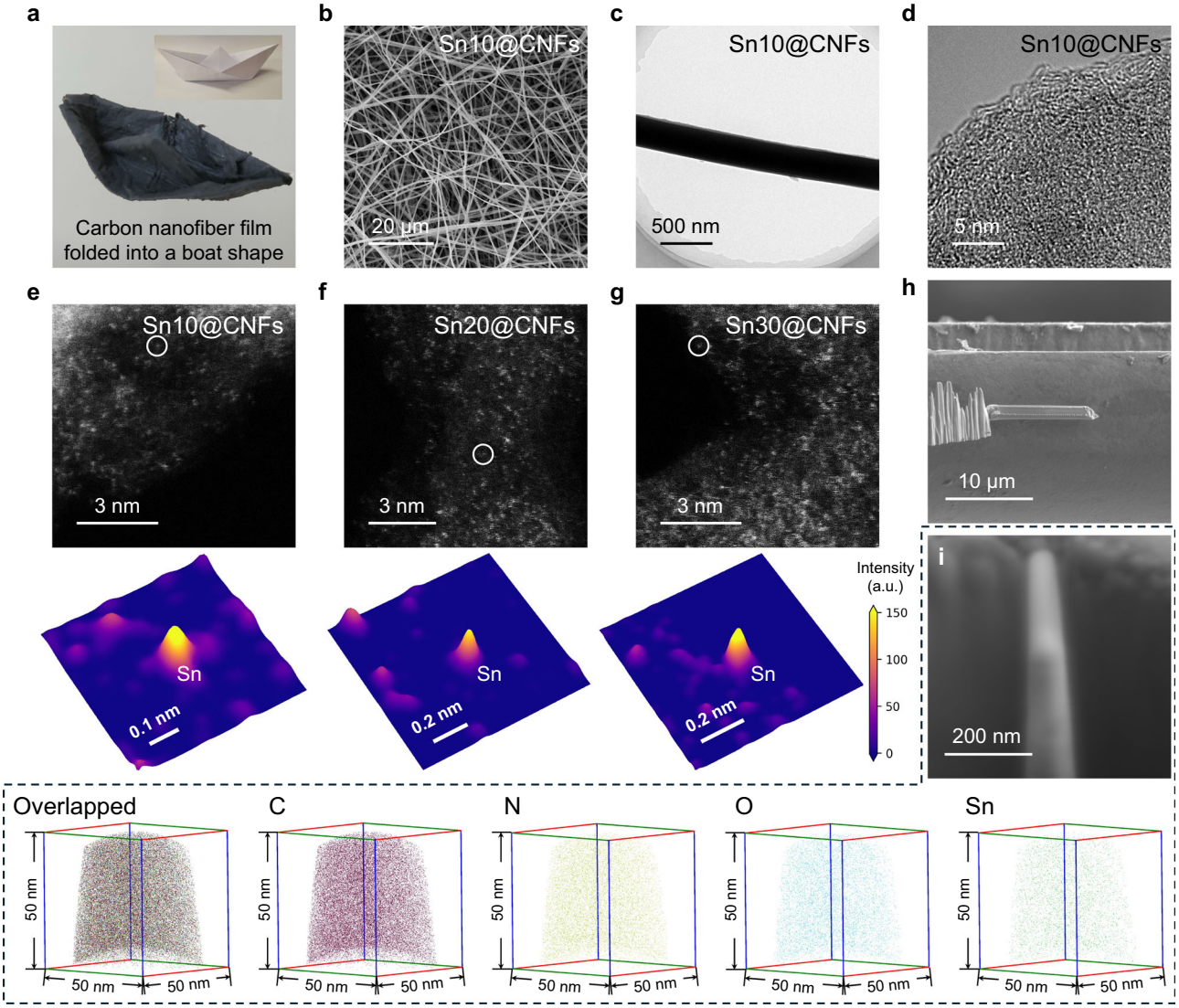

Fig. 1 | Morphology and microstructure of carbon nanofibers. a Optical photo of a Sn30@CNFs film folded into a boat shape. **b** SEM, **c** TEM, and **d** HRTEM images of Sn10@CNFs. AC-STEM images together with 3D profiles of the local structure of Sn atoms of **e** Sn10@CNFs, **f** Sn20@CNFs, **g** Sn30@CNFs. **h** FIB processing of Sn10@CNFs for APT. **i** SEM image of the prepared Sn10@CNFs sample for APT test and the corresponding results of 3D atomic distributions of C, N, O, and Sn elements.

coordination environment of Sn atoms transforms from 3N-Sn-O to 2N-Sn-2O and eventually to N-Sn-3O, demonstrating a Sn-concentration-dependent transition. This enables the controllable synthesis of carbon hosts with an optimal Sn coordination mode for guiding sodium deposition. The coordination environment of Sn was preliminarily revealed by XPS (Fig. 2c, d and Supplementary Fig. 11) and soft X-ray absorption spectra (sXAS, Supplementary Fig. 13). With the introduction of Sn, the N 1*s* XPS spectra of SnX@CNFs shows a new peak at 399.0 eV, in addition to the characteristic peaks at 398.2, 399.8, and 400.8 eV (corresponding to the N-6, N-5, and N-Q, respectively) in CNFs, which indicates the coordination between Sn and N[47]. Similarly, the O 1*s* XPS spectra of SnX@CNFs also emerge a new peak at 530.8 eV, alongside the peaks at 532.3 and 538.2 eV, which are assigned to C = O and C-O configurations[48] In addition, the ^{13}C NMR spectra (Supplementary Fig. 14) for both CNFs and Sn10@CNFs show approaching chemical shift at around 112 ppm, assigned to sp^2 hybridized carbon[49,50], indicating that the electrons from Sn has tiny shielding effect on C, reflecting the absence of Sn-C coordination. Thus, the primary coordination shell of Sn atoms consists of N and O ligands. Furthermore, as the Sn content in the carbon framework increases, the proportion of N from Sn-N coordination decreases, while the proportion of O from Sn-O coordination increases (Fig. 2b; Supplementary Fig. 12 and Supplementary Table 2), indicating a gradual replacement of N atoms by O in the coordination environment of Sn.

X-ray absorption near-edge structure (XANES) and extended X-ray absorption fine structure (EXAFS) provide the confirmation of the concentration-dependent coordination of Sn atoms. The white line peaks in Sn K-edge XANES spectra of SnX@CNFs ($X \leq 30$) are positioned between those of Sn and SnO_2 (Fig. 2e and Supplementary Fig. 15), indicating the +2 valence states, consistent with Sn 3*d* XPS spectra (Supplementary Fig. 11)[15]. The Fourier transformed (FT) k^3-weighted EXAFS spectra of SnX@CNFs show a predominant R-spacing peak at ≈1.53 Å (Fig. 2f), distinct from both the Sn-Sn peak in metallic Sn and Sn-O characteristic peak of SnO_2, indicating that Sn exists in an N, O co-coordination state without agglomeration[51]. The peak position of O-Sn-N in the R-space gradually shifts to higher *R* value as the atomic concentration of Sn increases, indicating an enhanced anchoring effect of O on Sn atoms. Least-squares fitting of Sn K-edge EXAFS curves further confirm the concentration-dependent coordination of Sn, revealing an alternating anchoring

https://doi.org/10.1038/s41467-025-64351-9

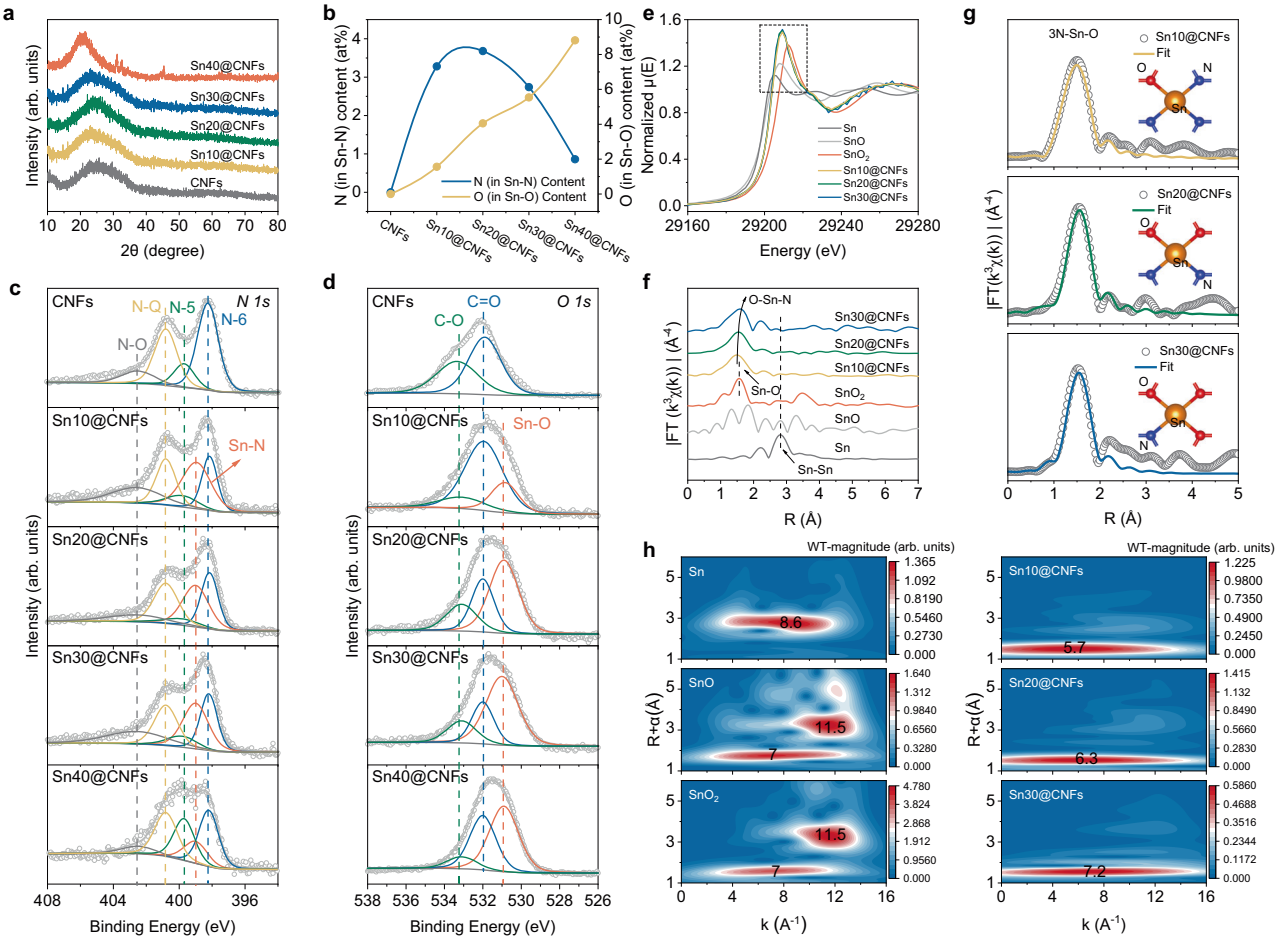

Fig. 2 | Structure and Sn coordination mode of carbon nanofibers. a PXRD patterns of carbon hosts with increasing Sn content. **b** The atomic content of N and O that coordinated with Sn obtained from high resolution **c** N 1*s* and **d** O 1*s* XPS of various carbon nanofibers. **e** Normalized Sn K-edge XANES (y-axis normalization is conducted by extrapolate both the pre-edge and post-edge background functions), **f** k3-weighted FT-EXAFS, **g** EXAFS fitting curves in R-space and **h** WT-EXAFS contour plots of Sn, SnO, SnO_2 and SnX@CNFs ($X = 10, 20, 30$). Source data are provided as a Source data file.

mechanism (Fig. 2g and Supplementary Fig. 16). At low Sn content (Sn10@CNFs), the coordination configuration of Sn is 3N-Sn-O. For Sn20@CNFs, this changes to 2N-Sn-2O, and as the concentration of single Sn atoms increases, more O atoms coordinate with Sn to form N-Sn-3O in Sn30@CNFs with the mean bond lengths of 2.07 and 2.10 Å for Sn-O and Sn-N, respectively (Supplementary Table 3). The reason for this coordination configuration transition is that, at high terminal temperature, SAs prefer to coordinate with N, however, when increasing the amount of Sn source, the average amount of N bonding with each Sn decreases, resulting in a lower N/Sn ratio for each defect. Notably, the EXAFS curves of Sn, SnO, and SnO_2 standard samples are also fitted in Supplementary Fig. 17. The peaks in EXAFS spectra of Sn reference are fitted as Sn-Sn scattering path (Supplementary Table 4), revealing the absence of Sn clusters in all SnX@CNFs samples. Both the EXAFS fitting curves of SnO and SnO_2 show different dominant peaks from those of all SnX@CNFs samples, indicating the Sn atoms in SnX@CNFs also do not exist in the form of SnO and SnO_2. Furthermore, the wavelet transform-EXAFS (WT-EXAFS, Fig. 2h) with high resolution of both k and R spaces shows a shift in the maximum from 5.7 $Å^{-1}$ for Sn10@CNFs to 7.2 $Å^{-1}$ for Sn30@CNFs, which are significantly different from those recorded from Sn foil (Sn-Sn at 8.6 $Å^{-1}$), SnO and SnO_2 (7.0 and 11.5 $Å^{-1}$ arose from Sn-O and Sn-Sn, respectively), indicating the offset of the bond position arises from the influence of the coordination configurations.

Activation effect of Sn on surrounding structures

Encouraged by the controllable coordination mode of Sn, the plating/stripping process of Na on the as-prepared carbon textures is expected to be optimized precisely. Density functional theory (DFT) calculations were initially performed to investigate the adsorption energies of Na atoms on SnX@CNFs. According to the experimental Sn coordination structures, three $C_{44}N_xO_ySn$ models were optimized on the base of the pristine model, a 5 × 5 supercell of graphene containing 50 C atoms (Supplementary Data 1), as shown in Fig. 3a–d and Supplementary Fig. 19. For comparison, corresponding $C_{44}N_xO_y$ models without Sn atom were also established (Supplementary Fig. 18). Sodium atoms are respectively placed at different adsorption sites numbered from 1 to 26 for calculation.

Except its own sodium adsorption activity, Sn atoms can activate the surrounding carbon structure, and its active effect is dominated by the coordination environment. The graphite-like sodiophobic carbon network is thermodynamically unfavorable for Na adsorption. In the $C_{44}N_xO_y$ models (Supplementary Fig. 18 and Fig. 3e–h), apart from several adsorption sites located around the N_x-O_y macrocycle showing notably negative adsorption energies (E_{ad}), the remaining adsorption sites exhibit a weak adsorption activity, indicating the non-spontaneous adsorption process. In contrast, the introduction of Sn atoms greatly enhances the Na adsorption capability of all C44NxOySn models. Sn atoms themselves exhibit high Na affinity. The E_{ad} values of the sites located on top of Sn (No. 26 in Fig. 3a, d and No. 16 in Fig. 3b,

https://doi.org/10.1038/s41467-025-64351-9

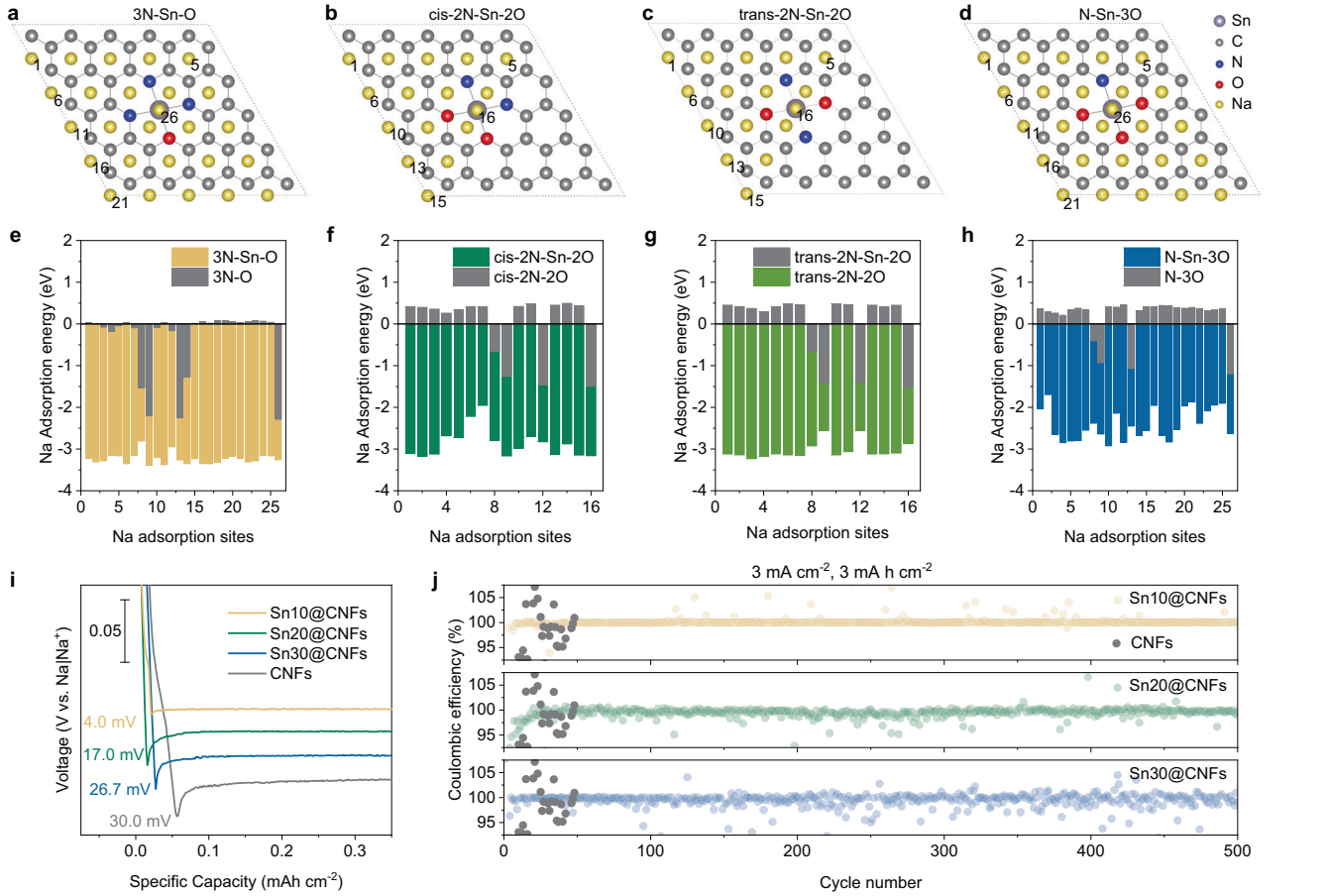

Fig. 3 | Sodium adsorption energy and nucleation barrier. Top view of two-dimensional **a** $C_{44}N_3OSn$, **b** $C_{44}N_2O_2Sn$ (cis), **c** $C_{44}N_2O_2Sn$ (trans) and **d** $C_{44}NO_3Sn$. DFT calculated Na adsorption energies on various adsorption sites on **e** $C_{44}N_3OSn$, **f** $C_{44}N_2O_2Sn$ (cis), **g** $C_{44}N_2O_2Sn$ (trans) and **h** $C_{44}NO_3Sn$. **i** Nucleation overpotential of CNFs and SnX@CNFs ($X = 10$, 20, and 30) under the current density of 0.5 mA cm^{-2}. **j** Coulombic efficiency of different electrodes in half cells under a deposition capacity of 3 mA h cm^{-2} with a current density of 3 mA cm^{-2}. Source data are provided as a Source data file.

c) is much lower than those at the same sites in the $C_{44}N_xO_y$. Similarly, the E_{ad} of hollow sites in the four heterocycles connected to Sn is reduced. More interestingly, Sn atoms can activate surrounding inert sites. In the $C_{44}N_xO_ySn$ models, the hollow sites of heterocycles not connected to Sn (N hollow or O hollow), and even the carbon hollow sites far from Sn atoms, exhibit lower E_{ad}, demonstrating a Na adsorption activity, while these sites in the $C_{44}N_xO_y$ models exhibit a thermodynamic disadvantage of Na^+ adsorption. The activation of Sn on surrounding structures creates additional active sites for Na adsorption. Furthermore, the average Na^+ adsorption energy on 3N-Sn-O sites surpass those of cis-2N-Sn-2O, trans-2N-Sn-2O and N-Sn-3O, emphasizing the importance of coordination configuration on Na^+ adsorption.

The experimental results regarding Na plating/stripping dynamics on SnX@CNFs provide further confirmation of the theoretical calculations. Nucleation overpotential reflects the energy barrier of initial Na deposition, lower value suggests improved Na affinity of the hosts[52]. Among all samples, at three different current densities, 0.5 mA h cm^{-2} (Fig. 3i and Supplementary Fig. 20), 1 mA h cm^{-2} (Supplementary Fig. 21) and 3 mA h cm^{-2} (Supplementary Fig. 22), Sn10@CNFs (3N-Sn-O structure) shows a lower value than Sn20@CNFs (2N-Sn-2O) and Sn30@CNFs (N-Sn-3O). Although Sn30@CNFs have the highest loading mass of Sn single atoms, the increasing of single atom concentration did not further contribute to lower nucleation overpotential, which indicates there is another more important factor affecting overpotential than single atom content, emphasizing the importance of optimizing the coordination structure. Moreover, the cycling stability of SnX@CNFs hosts in half cells also correlates with the Sn excitation capabilities, which is dominated by its coordination environment. Under a low current density (0.5 or 1 mA cm^{-2}) with a deposition capacity of 0.5 or 1 mA h cm^{-2}, all the SnX@CNFs ($X = 10$, 20, and 30) exhibit a better plating/stripping stability with a cycle life of 2000 h compared with the original CNFs (Supplementary Figs. 20 and 21). At higher current density of 3 mA cm^{-2} and higher capacity of 3 mA h cm^{-2} (Fig. 3j), Sn10@CNFs electrode shows the most stable cycling performance with the average coulombic efficiency (CE) stabilizing at 100.0%. While, although the cycle life of Sn30@CNFs is also expanded, the fluctuating CE reflects a relative high nucleation barrier and incomplete stripping process (average CE: 99.5%). Thus, among all structures, Sn atoms can activate the surrounding structures, turning the inert position to activity sites, and Sn coordinated with more N atoms (3N-Sn-O structure) can further improve the nucleation behavior of Na.

The activation effect of Sn on surrounding structures arises from the strong metal-support interaction in the form of the injection of Sn valence electrons into the π orbitals of the carbon matrix[53]. The Bader charge analysis directly reveals the electron transfer of Sn with O_xN_{4-x}-C (Supplementary Fig. 23). For Sn coordinated with more N atoms (3N-Sn-O), the higher charge suggests that the negatively charged N atoms draw electrons from Sn[54]. While for Sn coordinated with more O atoms (N-Sn-3O), the charge transfer between Sn and O is weaker, resulting in a relatively low Sn charge. Consequently, with the increase of O ligand

https://doi.org/10.1038/s41467-025-64351-9

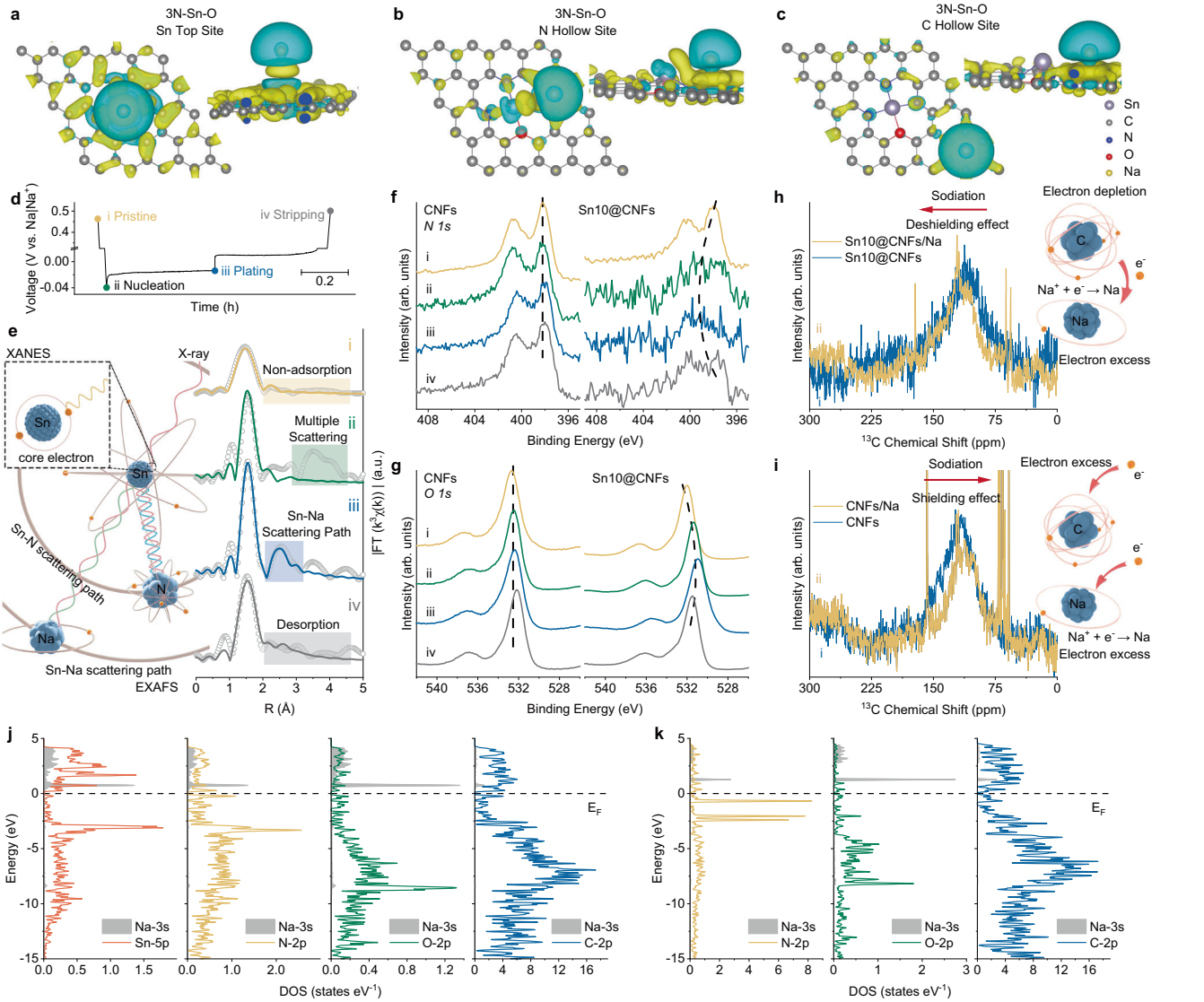

Fig. 4 | Sodium adsorption behavior of multi-stage active sites. Charge density difference iso-surfaces for the two-dimensional $C_{44}N_3OSn$ models before and after Na atom adsorbed ($\Delta\rho = \rho_{host-Na} - \rho_{host} - \rho_{Na}$, with value of 0.001 eBohr^{-3}, the yellow and blue colors indicate density excess and depletion, respectively) at **a** Sn site, **b** center of the C_5N ring and **c** center of the C_6 ring. **d** Plating/stripping voltage-time profile with charge/discharge states labeled under the current density of 0.5 mA cm^{-2} and a deposition capacity of 0.5 mA h cm^{-2} (i: pristine, ii: nucleation, iii: plating and iv: stripping). **e** Sn K-edge k^3-weighted FT-EXAFS fitting curves (R-space) corresponding to the states in (**d**). High resolution **f** N 1*s* and **g** O 1*s* XPS spectra of CNFs and Sn10@CNFs at different states. ^{13}C ssNMR spectra of **h** Sn10@CNFs and **i** CNFs under the states of pristine and nucleation. PDOS of **j** Sn, N, O, C in $C_{44}N_3OSn$ and **k** N, O, C in $C_{44}N_3O$ models after absorbing Na. Source data are provided as a Source data file.

in the coordination environment, the activating capability of Sn gradually decreases, because the charge transfer between Sn and O is weaker than that of Sn and N. Thus, Sn coordinated with more N atoms shows a stronger interaction with the support carbon matrix.

Sn activated multi-stage Na adsorption mechanism

The Sn10@CNFs with optimized coordination configuration (3N-Sn-O) were selected to study the sodium adsorption mechanism. Multi-stage active sites are used to describe the adsorption positions of $C_{44}N_3OSn$ model (Fig. 4a–c, Stage I: the top site of atomic Sn, Stage II: the surrounding hollow sites of Sn, such as those containing N and O atoms, Stage III: hollow sites composed solely of C atoms). Charge density difference reveals the adsorption of Na on the Stage I site (Fig. 4a). Electron depletion around Na^+ and accumulation around $C_{44}N_3OSn$ reflect a strong interaction between Na^+ and the carbon matrix via Sn, indicating the effective absorbance of Na on this active site[7]. Experimentally, Sn10@CNFs exhibits an upward edge energy shift after sodiation in ex situ XANES (Supplementary Fig. 24), reflecting the charge transfer happens between Na and Sn. FT-EXAFS depicts detailed information about the interactions between Sn and Na atoms at different plating/stripping states (Fig. 4d). Upon Na nucleation (Fig. 4e), a predominant R-spacing peak emerges at ≈3.4 Å, which is distinguished from single scattering because it is longer than the Sn-Sn scattering path and thus attributed to second shell or multiple scattering. After plating 0.5 mA h cm^{-2} of Na, a neo-peak appears at ≈2.5 Å in R-space, which is absent in Sn, SnO, SnO_2 and various pristine SnX@CNFs. Fitting analysis attributes this peak to the Sn-Na scattering path, confirming the interaction between Sn active site and Na^+. The Sn-Na scattering path completely disappears after charging, indicating the complete stripping.

The Na adsorption on the Stage II sites was first explored by charge density difference (Fig. 4b). Electron depletion around N and O was observed after Na adsorption, indicating the interaction between Na and N. The shift of N 1*s* peaks in XPS towards higher binding energy

upon Na plating (Fig. 4f) confirms this interaction, occurring specifically around the initial binding energy of 398.8 eV[55]. Given the proximity of Sn-N binding energy to this region, the involvement of Sn-coordinated nitrogen atoms in Na adsorption is confirmed[56,57]. Analogously, the obvious change of the dominant peak in O 1*s* XPS spectra also indicates the activity of O-configurations (Fig. 4g). Noticeably, at the stripping state, the influence of Na on the conjugated system is almost eliminated, manifested as the N 1*s* and O 1*s* binding energy returning to the initial position. As a comparison, the binding energies of N 1*s* and O 1*s* of CNFs show inconspicuous changes before and after Na plating, reflecting the Na-phobic property of N and O that were not coordinated with Sn. For Sn30@CNFs (N-Sn-3O configuration), although its N and O are active, the irreversible change of N 1*s* and O 1*s* binding energy reflect the incomplete sodium stripping (Supplementary Fig. 25), which is the root for the fluctuation of CE in half batteries with Sn30@CNFs electrode (Fig. 3j). In short, the reversible change in binding energy during plating/stripping processes of Sn10@CNFs reveals the Na^+ adsorption ability of N and O which constitutes the Stage II active sites.

Besides, the charge density difference after adsorbing Na^+ around the Stage III site hints the activity of carbon matrix (Fig. 4c). ^{13}C magic angle spinning solid-state nuclear magnetic resonance (MAS-ssNMR) spectroscopy was conducted to confirm the Na^+ adsorption process around C-contained structure (Fig. 4h). Different from the spectra of CNFs, where the ^{13}C chemical shift decreases after sodiation due to the shielding effect caused by electron accumulation (Fig. 4i), the ^{13}C chemical shift of Sn10@CNFs increases significantly after Na plating. This increase is attributed to the de-shielding effect of adsorbed Na^+ on C atoms, corresponding to the blue region adjacent to C atoms in Fig. 4a–c[58,59]. Notably, both CNFs and Sn10@CNFs show the peak locating at ca. 121 ppm which is attributed to the chemical shift of C in C=O after sodiation, indicating the carbonyl structure are similar in all samples, the movement of the chemical shift of the broad peak is not aroused from the C=O formation.

Projected density of states (PDOS) gives the confirmation of the interactions between Na^+ and Sn, N, O, C elements based on the optimized structures (Supplementary Data 1). Compared with the absence of PDOS overlapping between Na and N, O elements in unmodified $C_{44}N_xO_y$ models (Fig. 4k and Supplementary Fig. 26b, d), the activation effect of Sn towards the carbon matrix promoted the adsorption capacity of the originally inert sites for Na^+. For $C_{44}N_xO_ySn$ models after adsorbing Na (Fig. 4j and Supplementary Fig. 26a, c), the overlapping of electronic distribution regions in s orbitals for Na and p orbitals for C, N, O, and Sn directly reflect the binding formation, indicating all elements contribute to the Na^+ adsorption. Thus, except for the highly anticipated single atom sites themselves, the activation effect of single atoms on the surrounding structure is also crucial. In Sn single atom dispersed carbon texture, N, O, and C contribute abundant active sites and form multi-stage Na^+ adsorption sites.

Na nucleation and growth dynamics of Sn activated carbon host

Benefiting from the multi-stage active sites motivated by coordination-optimized Sn, uniform deposition and stripping performance were achieved under high current density. The ab initio molecular dynamics (AIMD) simulations were first conducted to reveal the homogenous deposition of Na on Sn-modified carbon texture. The simulations begin with a sparse distribution of Na atoms, followed by a sequential deposition of additional atoms on two models (Fig. 5a): one containing a defect with three nitrogen and one oxygen (3N-O) and the other with additional Sn atoms in the 3N-O model (3N-Sn-O). The initial and final configurations for the molecular dynamics trajectories are provided in Supplementary Data 2. AIMD simulation gives the result that, on the 3N-O model, the aggregation of Na was observed at as early as 10 ps, indicating Na nucleation prefers agglomerating as a cluster instead of uniform distribution. However, the absence of Na cluster aggregation in the 3N-Sn-O model during the simulation reflects the strong interaction between the 3N-Sn-O modified carbon texture and Na atoms, manifesting as dispersed and uniform nucleation. Thus, Sn activated carbon substrate is expected to correct the vertical growth into planar deposition, avoiding the dendrites formation.

As indicated by AIMD, the dendrite-free Na plating/stripping process along Sn-separated fibers was recorded by ex situ SEM and in situ optical microscope. On CNFs, the irregularly nucleated Na presents as agglomerated bulk, subsequently accumulating and aggregating on plated Na (Fig. 5b). This uneven deposition promotes dendrite formation, as observed in the in situ optical microscopy (Fig. 5c). Dendrites on CNFs appeared after 45 min of plating under 2 mA h cm^{-2}, and the formed dendrite detach from the host after 60 min, turning into dead Na. Furthermore, Na residues on stripped CNFs highlight the challenge of achieving complete stripping (Fig. 5b). In contrast, the nucleation performance of Sn-activated carbon skeletons is significantly improved. On both Sn10@CNFs (3N-Sn-O coordination, Fig. 5b) and Sn30@CNFs (N-Sn-3O structure, Supplementary Fig. 27), the Na accumulation process along the fibers reflects guidance for sodium deposition, which effectively utilizes the space of the 3D host. Even when uniformly grown Na completely fills the 3D network, the fiber morphology remains clearly visible without mossy Na dendrites in both top-view (Supplementary Fig. 28) and side-view (Supplementary Fig. 29). Meanwhile, the absence of dendrite formation observed on Sn10@CNFs during the electroplating process (Fig. 5c) further confirms that the sufficient multi-stage active sites break the tendency of sodium aggregation, transforming irregular nucleation into uniform deposition (Supplementary Fig. 30). Even when the deposition capacity is increased to 250 mA h cm^{-2} at a current density of 5 mA cm^{-2}, the capacity-voltage curve of the battery remains stable (Supplementary Fig. 31), and the morphology of plated Na is still flat (Supplementary Fig. 32), demonstrating the sodium affinity of the carbon skeleton. In short, dendrite-free fiber-guided nucleation morphology exhibits advantages during the plating/stripping process, allowing Sn10@CNFs to carry a high Na capacity and achieve complete stripping without residue.

Electrolyte consumption caused by unstable interface and side reactions is one of the key reasons for battery failure[60,61]. The interface morphology of stripped carbon hosts after one cycle was also recorded to reveal the surface reactions. For CNFs, the by-products composed of C, O, and Na with an unconsolidated structure between fibers were observed (Supplementary Fig. 33a–c). Conversely, no distinct surface structure differing from the compact matrix was observed on Sn10@CNFs after 1 plating/stripping cycle, indicating relatively weak surface side reactions (Supplementary Fig. 33d–f). However, with the migration of the Sn coordination environment, by-products reappear and become increasingly pronounced from Sn20@CNFs to Sn40@CNFs (Supplementary Fig. 33g–o). Depth profiling XPS provides detailed surface component information about the hosts after one cycle. For CNFs (Supplementary Fig. 34), the SEI generated by the decomposition of ether-based electrolytes is mainly composed of organic components (e.g., O=C-O, C=O and C-O), which is the root for the fluffy and porous structure (Supplementary Fig. 33b). However, the SEI of Sn10@CNFs is mainly accompanied by beneficial components (Supplementary Fig. 35), such as C-F and Na-F, corresponding to the close-packed surface observed under TEM (Supplementary Fig. 33e). For Sn30@CNFs, the reappearance of the fluffy structure composed of organic components (Supplementary Figs. 33k and 36) is one of the reasons for its relative unstable electrochemical performance.

Na plating/stripping performance of Sn activated carbon host

Symmetric cells were assembled to evaluate the long cycle plating/stripping stability of SnX@CNFs under a high DoD (100%). Supplementary Fig. 37 shows a comparison of the cycling stability of CNFs/Na and SnX@CNFs/Na electrodes at a current density of 10 mA cm^{-2} with a

https://doi.org/10.1038/s41467-025-64351-9

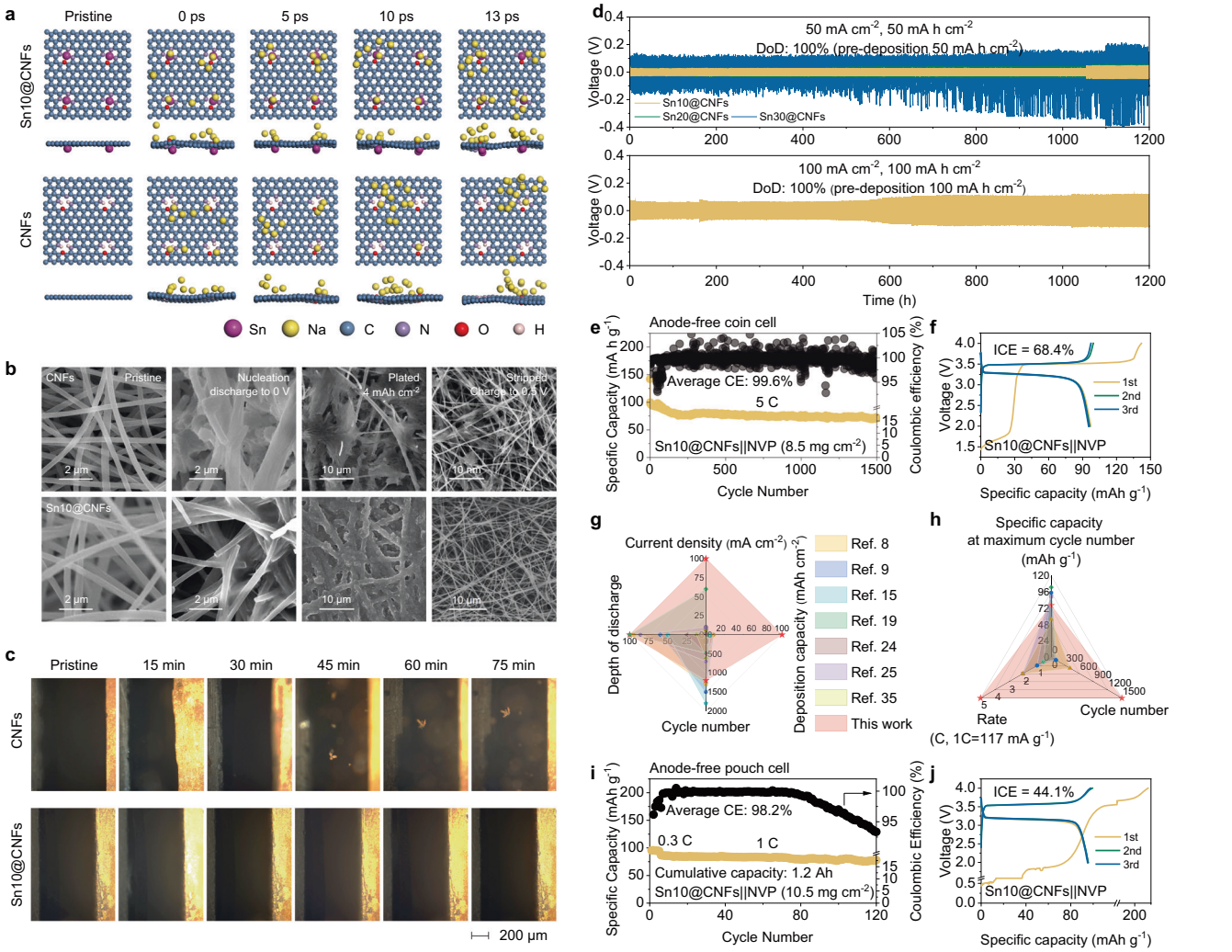

Fig. 5 | Sn-guided Na plating/stripping application performance. a Ab initio molecular dynamic simulation screenshots at different simulation times (0, 5, 10, and 13 ps) of the Sn10@CNFs and CNFs hosts. **b** SEM images of Sn10@CNFs and CNFs hosts under different plating/stripping states (operation current density: 0.5 mA cm^{-2} with maximum deposition capacity of 4 mA h cm^{-2}). **c** In situ optical microscope of the Sn10@CNFs and CNFs hosts at various deposition times (operation current density: 2 mA cm^{-2}). **d** Cycling performance of symmetric cells assembled by various electrodes pre-deposited with Na. **e** Cycling performance of anode-free Sn10@CNFs||NVP full cells under the charge/discharge rate of 5C (0.585 A g^{-1}) with **f** corresponding voltage profiles. Comparison of the properties of **g** symmetric cells and **h** anode-free full cells assembled by integrating Sn10@CNFs host and NVP cathode with some advanced sodium hosts/anodes[8,9,15,19,24,25,35]. The source of the literature data shown in this figure can be found in Supplementary Information, Supplementary Tables 5 and 6. **i** Cycling performance of anode-free Sn10@CNFs||NVP pouch cells under the charge/discharge rate of 1 C with **j** corresponding voltage profiles. Source data are provided as a Source data file.

fixed capacity of 10 mA h cm^{-2} (pre-deposition: 10 mA h cm^{-2}). The Sn10@CNFs/Na symmetric cells exhibit a relative constant voltage hysteresis of around 22 mV during its cycle life of 2800 h, which also reflects the diminishing side reactions on the interface. The Sn20@CNFs electrode, featuring a 2N-Sn-2O coordination mode exhibits higher voltage hysteresis with a slight increase. The cycle life of Sn30@CNFs/Na symmetric cell is limited by the significantly rising hysteresis voltage resulting from relatively intense side effects. In sharp contrast, the CNF/Na symmetric cells fail within a few dozen hours, characterized by massive irreversible side reactions and dendrite growth. At a high current density (50 mA h cm^{-2}) with a capacity of 50 mA h cm^{-2} (Fig. 5d and Supplementary Fig. 38), Sn10@CNFs/Na symmetric cells also demonstrate a long cycle life exceeding 1200 h under 100% DoD. When further increasing the fixed area capacity to 100 mA h cm^{-2}, Sn10@CNFs/Na symmetric cells can even operate at 100 mA cm^{-2} for 1200 h under fully stripped conditions with a tighter voltage hysteresis of around 70 mV, showcasing substantial advantages compared to other recently reported sodium hosts/anodes (Fig. 5g and Supplementary Table 5). Thus, the dendrite-free Sn10@CNFs electrode demonstrates a potential for application in sodium metal batteries (SMBs), benefiting from suppressed side reactions, enhanced sodiophilicity and regulated Na plating/stripping process.

The complete stripping performance of Sn10@CNFs underscores their application properties. Full cells were assembled by incorporating with SnX@CNFs/Na as the anode and NVP as the cathode (Supplementary Fig. 39). Upon overloading the pre-deposited Na on SnX@CNFs hosts, the charge/discharge profiles of Sn10@CNFs/Na||NVP full cells for the initial cycle at 100 mA g^{-1} show a reversible capacity of 105.8 mA h g^{-1} with the corresponding initial CE of 98.4% (Supplementary Fig. 40b). The Sn10@CNFs/Na||NVP full cells exhibit a high-rate performance with the specific capacities stable at 102.1, 99.8, 94.5, 89 mA h g^{-1} at 200 mA g^{-1}, 500 mA g^{-1}, 1000 mA g^{-1}, 2000 mA g^{-1} and 5000 mA g^{-1}, respectively, higher than those of the CNFs/Na||NVP full cells (Supplementary Fig. 40a). Furthermore, batteries with Sn10@CNFs/Na anodes can demonstrate a long cycle life in different

electrolytes, delivering a high discharge capacity of 84 mA h g^{-1} (Supplementary Fig. 41) after 2000 cycles at 1 A g^{-1}. In comparison, the capacity of Na||NVP cells rapidly decay to below 60 mA h g^{-1} after 570 cycles. Moreover, Sn10@CNFs/Na can withstand higher current density up to 2 A g^{-1}, with a capacity of 78 mA h g^{-1} after 2000 cycles (Supplementary Fig. 42b). The charge/discharge profiles show the characteristic of Na plating/stripping process on the anode of full-cell with overloaded Na (Supplementary Fig. 42a).

The above results indicate that Sn10@CNFs, serving as the host material for Na metal, are suitable for anode-free SMBs. When employing Sn10@CNFs without pre-deposition of Na as the host and high-loaded NVP (about 8.5 mg cm^{-2}) as the cathode, with sufficient electrolyte, the anode-free SMB shows stable cycling performance (1500 cycles) and competitive reversible capacity (73 mA h g^{-1}) under 5C (Fig. 5e). The "soft short" at the 1588th cycle (Supplementary Fig. 43b, c) indicates battery failure. The capacity loss of each cycle was summarized in Supplementary Fig. 43d, the average Na^+ consumption (within 1500 cycles) could be calculated as 0.003 mA h per cycle, corresponding to 0.05% of active Na^+ in electrolyte. Within 1500 cycles, the average CE of Sn10@CNFs||NVP anode-free SMB is 99.6%, the CE fluctuates with the range from 92 to 106% (Supplementary Fig. 43e, f). The dominant plateau region and limited slopping region (Fig. 5f) reflects the sodium is stored by being plated on the Sn10@CNFs hosts instead of being depleted on interphase[8]. Supplementary Fig. 44b shows the electrochemistry characteristic of sodium-ion batteries, showcasing as wide oxidation-reduction peaks in cyclic voltammetry (CV) curves and slope curves in the voltage profiles. In contrast, the electrochemical features of anode-free batteries are different, with sharp oxidation-reduction peaks in CV curves and sustained charge/discharge plateaus (Supplementary Fig. 45b). Even under the charge/discharge condition of 10 C (Supplementary Fig. 45d), the anode-free cells demonstrate a long cycle stability (700 cycles) with an average CE of 98.1% and a high specific capacity of 83 mA h g^{-1} in the last cycle. Moreover, even under 20 C (Supplementary Fig. 46), the Sn10@CNFs can support the battery operation for over 700 cycles with an average CE of 97.4%. Sn10@CNFs hosts provide a stable place for Na plating/stripping, enabling the slow Na^+ consumption to compensate Na^+ loss in irreversible plating/stripping (reflected by the charging capacity is slightly higher than the discharging capacity of the previous cycle). Because the charging capacity is slightly higher than the discharging capacity, the batteries can achieve a stable cycle under a CE less than 100% (Supplementary Table 7 and Supplementary Fig. 8). The performance of the anode-free batteries based on Sn10@CNFs host is comparable with most SMBs using NVP as cathode (Supplementary Table 6 and Fig. 5h).

To further emphasize the practicality of Sn10@CNFs hosts, we paired them with a different cathode material, $NaNi_{1/3}Fe_{1/3}Mn_{1/3}O_2$ (NFM) (Supplementary Fig. 47). The electrochemical performance of NFM in half cells is shown in Supplementary Fig. 48. In anode-free Sn10@CNFs||NFM cells (Supplementary Fig. 49), the Sn10@CNFs delivered stable cycling for 300 cycles at 1 C (138 mA h g^{-1}) and maintained meaningful performance even at 2 C (Supplementary Fig. 50). Overall, Sn10@CNFs effectively regulate Na deposition behavior, while the optimized Sn coordination structure suppresses surface side reactions, enabling 100% Na utilization under high deposition capacity and current density.

Anode-free pouch cells were assembled to further evaluate the suppression of dendrite formation and negligible side reactions on the Sn10@CNFs host, confirming its practical applicability (Supplementary Fig. 51). The Sn10@CNFs||NVP anode-free pouch cell, initially tested at 0.5 C (Supplementary Fig. 52), delivered a cumulative capacity (2.55 A h) with a cycle life of 200 cycles and an average CE of 98.1%. Even at a higher rate of 1 C (Fig. 5i), the cell maintained a cycle life of 120 cycles with an average CE of 98.2%. Charge/discharge profiles (Fig. 5j) indicate that Na plating/stripping is the primary contributor to capacity. At 1 C, the cumulative capacity of 1.2 A h is enabled by dendrite-free sodium deposition and minimal side reactions, effectively preventing short-circuiting and capacity degradation.

Discussion

In summary, we have developed a coordination-controllable carbon host with atomically dispersed Sn to guide homogenous Na deposition in three dimensions and elucidated both the intrinsic activity of Sn single atoms and their activation effect on the surrounding structure. Sn was confirmed to exist in an atomically isolated state within the carbon matrix, and increasing Sn loading induced a concentration-dependent shift in coordination mode from 3N-Sn-O to N-Sn-3O. The introduction of Sn single atoms enhances the sodium affinity of carbon matrix, which is not only attributed to the activity of Sn single atoms themselves, but also contributed from the surrounding structure (heteroatoms coordinate with Sn and carbon skeleton) activated by Sn. Replacement of N with O in the coordination environment was found to impair Na adsorption. EXAFS, XPS, and NMR analyses revealed multi-stage active sites for Na adsorption during plating/stripping, where initially inert sites become activated by Sn to bind Na^+. The Sn-activated carbon framework effectively directs Na deposition, enabling dendrite-free growth along the fibers and complete stripping with 100% Na utilization. In symmetry cells, Sn10@CNFs/Na electrode operated over 1200 h at a high current density of 100 mA h cm^{-2} and a capacity of 100 mA h cm^{-2} with 100% DoD. Sn10@CNFs/Na||NVP full cells delivered 78 mA h g^{-1} after 2000 cycles at 2 A g^{-1}, while anode-free Sn10@CNF||NVP cell achieved 83 mA h g^{-1} after 700 cycles at 10 C. Overall, this work offers a strategy to regulate Na^+-carbon interactions, providing insights for the safe and high-performance operation of sodium metal-based batteries.

Methods

Preparation of carbon nanofibers

The Sn-doped nanofibers were prepared by a single-nozzle electrospinning method with the following carbonization. Firstly, 1.264 g of PAN (M_w = 150,000, J&K Scientific) was dissolved in N, N-dimethylformamide (≥99.9%, J&K Scientific) to obtain 10 wt% PAN solution. Then, 0.13, 0.25, 0.38, and 0.51 g of $SnCl_2{\cdot}2H_2O$ (≥99.8%, Sinopharm Chemical Reagent Co., Ltd) was added into the above solution, which was subsequently stirred at 50 °C for 5 h to obtain a mixture for electrospinning. After that, the solution obtained was transformed into a 5 mL syringe with a 23 gauged stainless-steel needle. Under the voltage of 25 kV, the distance of 20 cm was maintained between the tip of the spinneret and the collector. Next, as-collected fibers were dried in air at 80 °C for 12 h to evaporate the solvent. For carbonization, the nanofiber films were stabilized in air at 265 °C with a heating rate of 1 °C min^{-1} for 2 h at first. Thereafter, the precursors were annealed in a N_2 flow at 800 °C for 1 h with a heating rate of 5 °C min^{-1}. According to the weight fraction of $SnCl_2$ in the precursor, the samples were donated as Sn10@CNFs, Sn20@CNFs, Sn30@CNFs and Sn40@CNFs. The non-doped carbon nanofibers were prepared by the same processes, named as CNFs.

Preparation of $Na_3V_2(PO_4)_3$

NVP cathode active materials for full cells were prepared by the sol–gel method. 0.1 M of NH_4VO_3 (≥99%, Aladdin), 0.15 M $NH_4H_2PO_4$ (≥99%, Aladdin), 0.15 M NaOH (≥97%, Aladdin), and 0.1 M citric (≥99.5%, Aladdin) acid were firstly dissolved in 80 mL of deionized water. The solution obtained was subsequently evaporated at 80 °C with stirring for 12 h. Next, the mixture was heated to 800 °C with a heating rate of 5 °C min^{-1} in an argon atmosphere and then kept at 800 °C for 9 h before naturally cooling to room temperature to obtain NVP.

Positive electrode preparation

NVP or NFM (Shenzhen Kejing STAR Tech Co., Ltd.), acetylene black (Canrd Technology Co. Ltd.), and PVDF (≥99.5%, Canrd Technology Co. Ltd.) were mixed in an 8:1:1 weight ratio with N-methyl-2-pyrrolidone (NMP, 99.5%, Beijing Tongguang Fine Chemical Company) as the solvent. The slurry was prepared in air (25 ± 10 °C) using a mortar and pestle, cast onto Al foil (>99.9%, 16 μm, HF-Kejing Materials Tech Co., Ltd.) with a doctor blade, and dried overnight at 100 °C.

Material characterizations

The field emission scanning electron microscope images were recorded by Hitachi S-4700 microscope. The transmission electron microscopy (TEM), HRTEM and HAADF-STEM images were obtained on Tecnai G2F20 UTWIN electron microscope equipped with EDX spectroscopy (Oxford) to perform elemental analysis, using an accelerating voltage of 300 kV. Aberration-corrected scanning transmission electron microscope (AC-STEM) was performed on a JEOL JEM-ARM200F TEM/STEM with a spherical aberration corrector, operated at 200 kV. The samples for AC-STEM are prepared by ball milling following with ultrasonic dispersion in ethanol. Sample preparation and APT measurement are performed according to the literature[62]. The Sn10@CNFs were mixed with photosensitive resin and then cleaned and dried on a Si substrate before sputter coating with Cr. Thermo Fisher Scientific Helios 5UC DualBeam FIB-SEM was used to fabricate the apex. APT were performed with a local electrode atom probe (CAMECA LEAP 5000XR) under a laser mode. Ultraviolet laser pulsing at laser energy of 50 pJ, a pulse repetition rate of 200 Da, and a target evaporation rate of 1.0% per pulse at 40 K. The reconstruction of the APT data were performed using CAMECA IVAS6 software. The Brunauer–Emmet–Teller surface area was obtained by isothermal nitrogen adsorption/desorption measurements on an ASAP 2020 (Micromeritics) at 77 K. Raman spectra were recorded in the range of 500–2000 cm^{-1} by a JY HR800 Raman spectrometer with a 532 nm laser excitation. TG analysis was studied using Netzsch STA 449C with a heating rate of 10 °C/min in oxygen atmosphere. XRD patterns were collected on Rigaku D/max-2500B2+/PCX, using the Cu Ka radiation (λ = 0.154 nm) within a 2-theta angle range from 5 to 90°. XPS were recorded by a Thermo Electron Corporation ESCALAB 250 XPS spectrometer, using monochromatized Al Kα radiation (1486.6 eV) with 30 eV pass energy in 0.5 eV steps over a sample area of 650 × 650 μm under high vacuum (<10^{-7} Pa). ^{13}C MAS-ssNMR were recorded by a Bruker Avance III 400 NMR spectrometer, with conductive samples mixed with KBr (1:5). To collect carbon hosts plated with Na for ex situ XPS and ex situ ssNMR tests, approximately 100 half cells were assembled. Sodiation was performed by discharging the cells to 0 V at 0.565 mA cm^{-2}. All sample preparation was conducted in an argon-filled glove box with water and oxygen levels below 0.1 ppm to prevent contamination. Electrodes were retrieved from the cells, ground into powder, and then loaded either into sealing-film-sealed ssNMR tubes or mounted on conductive adhesive (stored in sealed plastic bags prior to testing). Sample transfers were performed using argon-filled sealed containers to avoid air exposure. sXAS were measured at beamline BL12B of the National Synchrotron Radiation Laboratory of China with a step length of 0.05 eV under the pressure of 10^{-10} Torr and total electron yield mode. Sn K-edge X-ray absorption fine structure (XAFS) spectra were acquired in fluorescence mode using a seven-element silicon drift detector with photon fluxes ranging from 1.8×10^{10} to 2×10^{8} photons per second under high energy mode. For ex situ XAFS, half cells were discharged/charged to target voltages and then disassembled inside the argon glove box. Electrodes were covered on all surfaces and edges with Kapton tape and stored in argon-filled sealed containers during transport and measurement, preventing air exposure. In situ optical microscope was performed on OLYMPUS BX51M polarization microscope. A specialized two electrode battery with a quartz window was charged/discharged at 2 mA cm^{-2} to observe dendrite growth, using Na (12 mm diameter, ~200 μm thick) as the negative electrode and Sn10@CNFs (12 mm, ~4 mg cm^{-2}, ~200 μm thick) as the positive electrode.

Cells assembly and measurements

Coin cells (CR2032) and pouch cells were assembled/disassembled in an argon-filled glove box (H_2O and O_2 < 0.1 ppm). A single layer of glass fiber separator (Whatman GF/D, 16 mm diameter, 0.68 mm thickness, 2.7 μm pore size, 40–50% porosity) was cut using an MSK-T10 manual slicer (Shenzhen Kejing STAR Tech Co., Ltd.). Electrolytes for half and symmetric cells were 200 μL of 1.5 M sodium triflate ($NaCF_3SO_3$) in diglyme (DoDoChem, ≥99.8%), while full cells used 200 μL of 1 M $NaPF_6$ in diglyme (DoDoChem, ≥99.8%). Electrolytes were stored in aluminum bottles inside the glove box and transferred using polypropylene pipette tips. All electrochemical measurements were performed at ambient temperature (25 ± 10 °C) without thermal or environmental control. Tests were conducted on a battery test system (LANHE CT2001A). Potentiostatic electrochemical impedance spectroscopy (EIS) was collected on a CHI660E electrochemical workstation using a 50 mV AC amplitude with alogarithmic frequency distribution of 6 points per decade in the frequency range from 1 to 100 MHz. The time applied during open-circuit potential before carrying out EIS test was 60 s. The CV was tested on a CHI660E electrochemical workstation in the cell voltage range of 2–4 V, and the scanning rate was 0.1 mV s^{-1}.

Half cells. CNFs were cut into discs with a diameter of 12 mm as the working electrode with the mass loading of 0.4–0.8 mg cm^{-2} (20–40 μm thickness). Na metal (Aladdin, >99.7%) served as the counter electrode, prepared by rolling Na ingots into ~200 μm foils, cutting into 14 mm discs without specific surface treatment. Cells were activated for 10 cycles at 0.113 mA (0.1 mA cm^{-2}) between 0 and 0.5 V (vs. Na/Na^+) before testing. In each cycle, Na plating/stripping was performed at 0.5, 1, and 3 mA cm^{-2} to deposition capacity of 0.5, 1, and 3 mA h cm^{-2}, followed by stripping to 0.5 V vs. Na^+/Na. Current density was calculated based on the CNF area (1.13 cm^2).

Symmetric cells. Na was pre-deposited on CNFs (12 mm of diameter, 3.5–4 mg cm^{-2}, ~200 μm thickness) in half cells using Na foil (~1 mm thickness) at 1 or 2 mA cm^{-2} to capacities of 10, 50, and 100 mA h cm^{-2}. Subsequently, these pre-deposited CNFs were then assembled into symmetrical cells, cycled at 10, 50, and 100 mA cm^{-2} for 1 h discharge/1 h charge.

Sodium-metal full cells. Electrolytes were 200 μL of 1 M $NaPF_6$ in diglyme or 1 M $NaClO_4$ in ethylene carbonate, dimethyl carbonate, and methyl ethyl carbonate (EC/DMC/EMC, 1:1:1 v/v) with 5% fluoroethylene carbonate (DoDoChem, ≥99.8%). Positive electrodes were 12 mm diameter discs with the mass loading of about 1.1 mg cm^{-2} (~40 μm thickness). For negative electrodes, CNFs (12 mm diameter, ~0.4 mg cm^{-2}, ~20 μm thickness) were pre-deposited with Na at 1 mA $cm^{-2}$to 6 mA h cm^{-2} before assembling full cells. Full cells were charged/discharged at 1 or 2 A g^{-1} between 2 and 4 V.

Sodium-ion full cells. Positive electrodes (12 mm diameter, 1.4 mg cm^{-2}, ~50 μm thickness) were prepared as above. CNFs (12 mm diameter, ~2 mg cm^{-2}, ~100 μm thickness) were pre-cycled in half cells for 5 cycles between 0 and 2.8 V (vs. Na/Na^+) at 0.5 mA cm^{-2} before full-cell assembly. Full cells were charged/discharged at 5 C between 2 and 4 V (1 C = 117 mA g^{-1}).

Anode-free full cells. Positive electrodes (12 mm diameter, 8.5 mg cm^{-2}, ~300 μm thickness). were prepared as above. For negative electrode side, CNFs (12 mm diameter, ~0.4 mg cm^{-2}, ~20 μm thickness) were pre-cycled in half cells for 10 cycles at 0.565 mA cm^{-2} between 0 and 0.5 V (vs. Na/Na^+) before full-cell assembly, no pre-

deposition of Na. And then, these CNFs and NVP (N/P ratio ~0.035) were used to assemble the anode-free full cells. Full cells were charged/discharged at the charge/discharge rate of 5 C, 10 C, 20 C between the cell voltage of 2–4 V (1 C = 117 mA g^{-1}).

Anode-free pouch cells. Single-layer anode-free pouch cells were assembled by pairing one NVP positive electrode (3 × 4 cm, 10.5 mg cm^{-2}, ~360 µm thickness) with one CNF negative electrode (3 × 4 cm, 0.4 mg cm^{-2}, ~20 µm thickness) and a sandwich-structured separator (Whatman GF/D, 3 × 4 cm) soaked in 1000 µL of 1 M $NaPF_6$ dissolved in diglyme (N/P ratio ~0.039). The assembly was packaged in Al-plastic films, with Al tabs (≥99.3%, Shenzhen Kejing STAR Tech Co., Ltd.) for the positive electrode and Ni tabs (≥99.6%, Shenzhen Kejing STAR Tech Co., Ltd.) for the negative electrode. Gas release was performed by evacuating to −95 kPa. For the negative electrode, CNFs were mixed with acetylene black (Canrd Technology Co. Ltd.), and poly (vinylidene fluoride) (PVDF, Kynar) in a weight ratio of 8:1:1, using NMP (99.5%, Beijing Tongguang Fine Chemical Company) as solvent. The slurry was prepared with a mortar with pestle in air (25 ± 10 °C), cast onto Cu foil (>99.9%, 25 µm thickness, HF-Kejing Materials Tech Co., Ltd.) via a doctor blade, and dried at 100 °C overnight. CNFs were electrochemically activated in half-pouch cells between 0 and 0.5 V (vs. Na/Na^+) for 1 cycle at 0.1 mA cm^{-2} without pre-deposition. For electrochemical testing, full pouch cells were initially cycled at 0.5 C for five cycles, followed by cycling at 0.5 or 1 C between 2 and 4 V. Specific capacity and current were calculated based on the NVP mass.

DFT calculations

Periodic spin-polarized DFT was applied to calculate changes in atomistic and electronic structures of the models for carbon hosts under the influence of sodium by using the plane-wave pseudopotentials[63,64] associated with the exchange-correlation formed by Perdew–Burke–Ernzerhof (PBE)[65,66] in the Vienna Ab initio Simulation Package[67]. The treated valence electrons for the C, O, N, Sn, and Na atoms are $2s^22p^2$ (ZVAL = 4.000), $2s^22p^4$ (ZVAL = 6.000), $2s^22p^3$ (ZVAL = 5.000), $5s^25p^2$ (ZVAL = 4.000) and $3s^1$ (ZVAL = 1.000), respectively. 3 × 3 × 1 Monkhorst-Pack k-point grid for the structural optimization and 5 × 5 × 1 mesh for the electronic structure calculations are set for the Brillouin zone sampling with the cut-off energy of 520 eV for plane wave expansion of the wave functions[68]. The convergence criteria for each self-consistent field cycle was set to 10^{-5} eV for total energy. The convergence criterion for each geometry optimization was set to 0.001 eV/Å for ionic forces.

A 5 × 5 supercell of graphene containing 50 C atoms was selected as the pristine model. Six models (i.e., $C_{44}N_3O$, $C_{44}N_2O_2$, $C_{44}NO_3$, $C_{44}N_3OSn$, $C_{44}N_2O_2Sn$, $C_{44}NO_3Sn$) are constructed and optimized based on it, according to the element ratio obtained from experiments. A vacuum region of at least 20 Å in the z-direction was constructed on the primary structural model and adsorption configurations to minimize the adjacent image interactions. Density of states and PDOS were calculated to quantify contributions from atomic orbitals to band structures. The adsorption energy (E_{ad}) of Na atom on $C_{44}O_xN_ySn$ and $C_{44}O_xN_y$ host was defined as:

$$E_{ad} = E_{\mathrm{Na-host}} - E_{\mathrm{host}} - E_{\mathrm{Na}} \quad (1)$$

where $E_{\mathrm{Na\text{-}host}}$ and E_{host} are the total energies of the corresponding hosts with and without adsorbed Na atom, respectively. E_{Na} is the average energy of metal Na.

To analysis the metal-support interaction, we performed Bader charge analysis on the converged charge densities. In addition, we constructed charge-density difference maps to further analysis charge transferred upon Na adsorption by subtracting the charge densities of Na atoms and each two-dimensional host without Na from the corresponding hosts with adsorbed Na atom.

$$\Delta\rho = \rho_{\mathrm{Na-host}} - \rho_{\mathrm{host}} - \rho_{\mathrm{Na}} \quad (2)$$

where $\rho_{\mathrm{Na-host}}$ is the charge density of hosts with Na atom, ρ_{host} is the charge density of two-dimensional hosts without Na atom, and ρ_{Na} is the charge density of Na atom.

Computational details for ab initio molecular dynamics simulations

The AIMD simulations in this work were conducted within the DFT, utilizing the Vienna Ab-initio Simulation Package[63]. The PBE form of generalized gradient approximation was selected as the exchange-correlation functional[67]. A plane-wave energy cutoff of 282 eV was chosen, along with the following projector augmented wave pseudopotentials: Sn_PBE ($5s^25p^2$) for tin, C_s ($2s^22p^2$) for carbon, N_s ($2s^22p^3$) for nitrogen, O_s ($2s^22p^4$) for oxygen, Na ($3s^1$) for sodium, and H_s ($1s^1$) for hydrogen[65]. A Monkhorst-Pack mesh with a k-point spacing of approximately $2\pi/30$ $Å^{-1}$ was employed with the supercell size is about 25 × 26 × 38 $Å^3$. The simulations were carried out with a time step of 1 fs for 13 ps under the canonical ensemble at an elevated temperature of 400 K. To model the Na deposition, Na atoms were gradually and randomly introduced into the system. We used hydrogen atoms to saturate the dangling bonds in 3N-O model, due to the dangling bonds were unstable, and hydrogen was ubiquitous in the experiment[69]. Additionally, considering that the valence of Sn in 3N-Sn-O model was +2 by Bader charge analysis, two hydrogen atoms were employed here.

Data availability

All data generated in this study are provided in the Supplementary Information/Source data file. Source data file has been deposited in Figshare under accession code DOI link[70].

References

1. Brunklaus, G., Lennartz, P. & Winter, M. Metal electrodes for next-generation rechargeable batteries. *Nat. Rev. Electr. Eng.* **1**, 79–92 (2024).
2. Lina, G., Juner, C., Qinlong, C. & Kong, X. The chemical evolution of solid electrolyte interface in sodium metal batteries. *Sci. Adv.* **8**, eabm4606 (2022).
3. Sun, J. et al. A phosphorene-graphene hybrid material as a high-capacity anode for sodium-ion batteries. *Nat. Nanotechnol.* **10**, 980–985 (2015).
4. Sayahpour, B. et al. Quantitative analysis of sodium metal deposition and interphase in Na metal batteries. *Energy Environ. Sci.* **17**, 1216–1228 (2024).
5. Mengqi, Z. et al. Homogeneous guiding deposition of sodium through main group II metals toward dendrite-free sodium anodes. *Sci. Adv.* **5**, eaau6264 (2019).
6. Xu, Z. et al. Homogenous metallic deposition regulated by defect-rich skeletons for sodium metal batteries. *Energy Environ. Sci.* **14**, 6381–6393 (2021).
7. Zhang, E. et al. Single-Atom yttrium engineering Janus electrode for rechargeable Na-S batteries. *J. Am. Chem. Soc.* **144**, 18995–19007 (2022).
8. Zhuang, R. et al. Fluorinated porous frameworks enable robust anode-less sodium metal batteries. *Sci. Adv.* **9**, eadh8060 (2023).
9. Wang, Y. et al. A sodium-antimony-telluride intermetallic allows sodium-metal cycling at 100% depth of discharge and as an anode-free metal battery. *Adv. Mater.* **34**, e2106005 (2022).
10. Hatzell, K. B. Anode-less or anode-free? *ACS Energy Lett.* **8**, 4775–4776 (2023).
11. Bai, M. et al. An anodeless, mechanically flexible and energy/power dense sodium battery prototype. *Energy Environ. Sci.* **15**, 4686–4699 (2022).

12. Zhang, Y. Y. et al. Refined electrolyte and interfacial chemistry toward realization of high-energy anode-free rechargeable sodium batteries. *J. Am. Chem. Soc.* **145**, 25643–25652 (2023).
13. Wang, Y. et al. Developments and perspectives on emerging high-energy-density sodium-metal batteries. *Chem*. **5**, 2547–2570 (2019).
14. Tomich, A. W. et al. A carboranyl electrolyte enabling highly reversible sodium metal anodes via a "fluorine-free" SEI. *Angew. Chem. Int. Ed.* **61**, e202208158 (2022).
15. Fei, X. et al. Atomic Sn–enabled high-utilization, large-capacity, and long-life Na anode. *Sci. Adv.* **8**, eabm7489 (2022).
16. Ye, L. et al. A sodiophilic interphase-mediated, dendrite-free anode with ultrahigh specific capacity for sodium-metal batteries. *Angew. Chem. Int. Ed.* **58**, 17054–17060 (2019).
17. Chu, C. et al. Recent advanced skeletons in sodium metal anodes. *Energy Environ. Sci.* **14**, 4318–4340 (2021).
18. Chen, Y. et al. Prospects for practical anode-free sodium batteries. *Mater. Today* **73**, 260–274 (2024).
19. Lee, K. et al. A 3D hierarchical host with enhanced sodiophilicity enabling anode-free sodium-metal batteries. *Adv. Mater.* **34**, e2109767 (2022).
20. Sun, Y., Li, J.-C., Zhou, H. & Guo, S. Wide-temperature-range sodium-metal batteries: from fundamentals and obstacles to optimization. *Energy Environ. Sci.* **16**, 4759–4811 (2023).
21. Chu, C. et al. Uniform nucleation of sodium in 3D carbon nanotube framework via oxygen doping for long-life and efficient Na metal anodes. *Energy Storage Mater.* **23**, 137–143 (2019).
22. Xu, Y. et al. Sodium deposition with a controlled location and orientation for dendrite-free sodium metal batteries. *Adv. Energy Mater.* **10**, 2002308 (2020).
23. Li, Z., Zhu, K., Liu, P. & Jiao, L. 3D confinement strategy for dendrite-free sodium metal batteries. *Adv. Energy Mater.* **12**, 2100359 (2021).
24. Mo, L. et al. Asymmetric sodiophilic host based on a Ag-modified carbon fiber framework for dendrite-free sodium metal anodes. *ACS Appl. Mater.* **13**, 48634–48642 (2021).
25. Li, S. et al. Space-confined guest synthesis to fabricate Sn-monodispersed N-doped mesoporous host toward anode-free Na batteries. *Adv. Mater.* **35**, e2301967 (2023).
26. Li, X. et al. An encapsulation-based sodium storage via Zn-single-atom implanted carbon nanotubes. *Adv. Mater.* **34**, e2202898 (2022).
27. Zhang, C. et al. Regulating the lithium ions' local coordination environment through designing a COF with single atomic Co site to achieve dendrite-free lithium-metal batteries. *Adv. Mater.* **35**, e2304511 (2023).
28. Qiao, B. et al. Single-atom catalysis of CO oxidation using Pt_1/FeOx. *Nat. Chem.* **3**, 634–641 (2011).
29. Wang, J. et al. Lithium atom surface diffusion and delocalized deposition propelled by atomic metal catalyst toward ultrahigh-capacity dendrite-free lithium anode. *Nano Lett.* **22**, 8008–8017 (2022).
30. Yang, Z. et al. Single-atom reversible lithiophilic sites toward stable lithium anodes. *Adv. Energy Mater.* **12**, 2103368 (2022).
31. Li, Y. et al. Single cobalt atoms decorated N-doped carbon polyhedron enabled dendrite-free sodium metal anode. *Small Methods* **5**, e2100833 (2021).
32. Zhai, P. et al. Uniform lithium deposition assisted by single-atom doping toward high-performance lithium metal anodes. *Adv. Energy Mater.* **9**, 1804019 (2019).
33. Chen, S. et al. Enabling low-temperature and high-rate Zn metal batteries by activating Zn nucleation with single-atomic sites. *ACS Energy Lett.* **7**, 4028–4035 (2022).
34. Chen, M. et al. Sn anodes protected by intermetallic $FeSn_2$ layers for long-lifespan sodium-ion batteries with high initial Coulombic efficiency of 93.8. *Angew. Chem. Int. Ed.* **62**, e202219177 (2023).
35. Li Y, et al. The sp hybridization of tin single atoms for dendrite-free sodium metal batteries. *Adv. Mater.* **37**, e2415026 (2025).
36. Xia, C. et al. General synthesis of single-atom catalysts with high metal loading using graphene quantum dots. *Nat. Chem.* **13**, 887–894 (2021).
37. Jing, T., Li, T., Rao, D., Wang, M. & Zuo, Y. Defining the loading of single-atom catalysts: weight fraction or atomic fraction? *Mater. Today Energy* **31**, 101197 (2023).
38. Wang, A., Li, J. & Zhang, T. Heterogeneous single-atom catalysis. *Nat. Rev. Chem.* **2**, 65–81 (2018).
39. Pei, J. et al. A replacement strategy for regulating local environment of single-atom Co-S_xN_{4-x} catalysts to facilitate CO_2 electroreduction. *Nat. Commun.* **15**, 416 (2024).
40. Zong, L. et al. Constructing Fe-N(4) sites through anion exchange-mediated transformation of Fe coordination environments in hierarchical carbon support for efficient oxygen reduction. *Angew. Chem. Int. Ed.* **62**, e202309784 (2023).
41. Wang, C. et al. Unveiling the effects of Cr single atoms with controllable configurations on solid electrolyte interphase and storage mechanism of sodium ions. *Adv. Funct. Mater.* **33**, 2214429 (2023).
42. Liu, J. C., Luo, F. & Li, J. Electrochemical potential-driven shift of frontier orbitals in M-N-C single-atom catalysts leading to inverted adsorption energies. *J. Am. Chem. Soc.* **145**, 25264–25273 (2023).
43. Xu, L. H., Liu, W. & Liu, K. Single atom environmental catalysis: influence of supports and coordination environments. *Adv. Funct. Mater.* **33**, 2304468 (2023).
44. Han, L. et al. A single-atom library for guided monometallic and concentration-complex multimetallic designs. *Nat. Mater.* **21**, 681–688 (2022).
45. Zhu, C., Usiskin, R. E., Yu, Y. & Maier, J. The nanoscale circuitry of battery electrodes. *Science* **358**, eaao2808 (2017).
46. Li, Y. et al. Origin of fast charging in hard carbon anodes. *Nat. Energy* **9**, 134–142 (2024).
47. Zhang, E. et al. Unraveling the capacitive charge storage mechanism of nitrogen-doped porous carbons by EQCM and ssNMR. *J. Am. Chem. Soc.* **144**, 14217–14225 (2022).
48. Tong, Y. et al. A bifunctional hybrid electrocatalyst for oxygen reduction and evolution: cobalt oxide nanoparticles strongly coupled to B,N-decorated graphene. *Angew. Chem. Int. Ed.* **56**, 7121–7125 (2017).
49. Walder, B. J. & Alam, T. M. Modes of disorder in poly(carbon monofluoride). *J. Am. Chem. Soc.* **143**, 11714–11733 (2021).
50. Wang, T. et al. Study of microstructure change of carbon nanofibers as binder-free anode for high-performance lithium-ion batteries. *ACS Appl. Mater.* **8**, 33091–33101 (2016).
51. Deng, Y. et al. Operando spectroscopic analysis of axial oxygen-coordinated single-Sn-atom sites for electrochemical CO_2 reduction. *J. Am. Chem. Soc.* **145**, 7242–7251 (2023).
52. Xie, C. et al. Microalloying induced stable welded interfaces for highly reversible zero-excess sodium metal batteries. *Energy Environ. Sci.* **17**, 4228–4237 (2024).
53. Xiao, C. et al. P-block tin single atom catalyst for improved electrochemistry in a lithium–sulfur battery: a theoretical and experimental study. *J. Mater. Chem. A* **10**, 3667–3677 (2022).
54. Qian, S. et al. Tailoring coordination environments of single-atom electrocatalysts for hydrogen evolution by topological heteroatom transfer. *Nat. Commun.* **15**, 2774 (2024).
55. Zhu, Q. et al. A 110 Wh kg^{-1} Ah-level anode-free sodium battery at −40 °C. *Joule* **8**, 482–495 (2024).
56. Zhao, Y. et al. Novel structural design and adsorption/insertion coordinating quasi-metallic Na storage mechanism toward high-performance hard carbon anode derived from carboxymethyl cellulose. *Small* **19**, e2303296 (2023).

57. Chen, R. et al. Amine-aldehyde condensation-derived N-doped hard carbon microspheres for high-capacity and robust sodium storage. *Small* **19**, e2303790 (2023).
58. Yu, Z. L. et al. Ion-catalyzed synthesis of microporous hard carbon embedded with expanded nanographite for enhanced lithium/sodium storage. *J. Am. Chem. Soc.* **138**, 14915–14922 (2016).
59. Svirinovsky-Arbeli, A., Carmieli, R. & Leskes, M. Multiple dynamic nuclear polarization mechanisms in carbonaceous materials: from exogenous to endogenous 13C dynamic nuclear polarization-nuclear magnetic resonance up to room temperature. *J. Phys. Chem. C* **126**, 12563–12574 (2022).
60. He, J. et al. Tuning the solvation structure with salts for stable sodium-metal batteries. *Nat. Energy* **9**, 446–456 (2024).
61. Wan, S. et al. Reductive competition effect-derived solid electrolyte interphase with evenly scattered inorganics enabling ultrahigh rate and long-life span sodium metal batteries. *J. Am. Chem. Soc.* **145**, 21661–21671 (2023).
62. Lei, Y. J. et al. Understanding the charge transfer effects of single atoms for boosting the performance of Na-S batteries. *Nat. Commun.* **15**, 3325 (2024).
63. Blöchl, P. E. Projector augmented-wave method. *Phys. Rev. B* **50**, 17953–17979 (1994).
64. Kresse, G. & Joubert, D. From ultrasoft pseudopotentials to the projector augmented-wave method. *Phys. Rev. B* **59**, 1758 (1999).
65. Kresse, G. & Furthmuller, J. Efficient iterative schemes for ab initio total-energy calculations using a plane-wave basis set. *Phys. Rev. B* **54**, 11169–11186 (1996).
66. Kresse, G. & Hafner, J. Ab initio molecular dynamics for liquid metals. *Phys. Rev. B* **47**, 558–561 (1993).
67. Perdew, J. P., Burke, K. & Ernzerhof, M. Generalized gradient approximation made simple. *Phys. Rev. Lett.* **77**, 3865–3868 (1996).
68. Monkhorst, H. J. & Pack, J. D. Special points for Brillouin-zone integrations. *Phys. Rev. B* **13**, 5188–5192 (1976).
69. Cheng, X. et al. Correlation between heteroatom coordination and hydrogen evolution for single-site Pt on carbon-based nanocages. *Angew. Chem. Int. Ed.* **63**, e202401304 (2024).
70. Gao S. et al. Single atom activated multi-stage active sites for thoroughgoing sodium utilization. figshare https://doi.org/10.6084/m9.figshare.28208822 (2025).

Acknowledgements

This work is supported by the National Natural Science Foundation of China (52173244 and 51872019, J.Z.), National Natural Science Foundation of China (12264029, J.H.), Jiangxi Province Natural Science Foundation (20242BAB25033, J.H.), Postdoctoral Fellowship Program of CPSF, China (GZB20230758, L.-N.W.), China Postdoctoral Science Foundation (2024M753237, L.-N.W.) and Fujian Key Laboratory of Green Extraction and High-value Utilization of New Energy Metals (2023-KFKT-2, L.-N.W.). B.L. acknowledges the financial support from the Australian Research Council (FT200100279). S.G. gratefully acknowledges the financial support from the China Scholarship Council (CSC). The authors appreciate the 4B9B Station of Beijing Synchrotron Radiation Facility (BSRF) and 11S2 XAS beamline of Aichi Synchrotron Radiation Center for their support. Part of this research was undertaken on the MEX-2 beamline at the Australian Synchrotron, part of ANSTO. The authors also appreciate the Taiyi cluster supported by the Center for Computational Science and Engineering of Southern University of Science and Technology for carrying the ab initio molecular dynamic simulations. The authors also acknowledge the scientific and technical support from the Australian Microscopy & Microanalysis Research Facility at the Centre for Microscopy and Microanalysis, the University of Queensland.

Author contributions

J.Z. provided the domain knowledge conceptualization. S.G., Y.-B.Z., and K.S. designed the methodology and performed the experiments. P.L., Y.-M.Z., and W.T. participated in the data analysis. J.H. conducted DFT calculations and L.-N.W. implemented the AIMD simulations. J.Z., Z.W., B.L., and L.-Z.W. supervised the project. All authors contributed to discussions and writing of the manuscript. S.G. and Y.-B.Z. contribute equally to this work.

Competing interests

The authors declare no competing interests.

Additional information

Supplementary information The online version contains supplementary material available at https://doi.org/10.1038/s41467-025-64351-9.

Correspondence and requests for materials should be addressed to Junping Hu, Lina Wang, Bin Luo or Jisheng Zhou.

Peer review information Nature Communications thanks the anonymous reviewer(s) for their contribution to the peer review of this work. [A peer review file is available].